

Roche tomography of cataclysmic variables – V. A high-latitude star-spot on RU Pegasi

A. Dunford^{1*}, C. A. Watson^{2†} and Robert Cannon Smith^{1‡}

¹*Astronomy Centre, University of Sussex, Falmer, Brighton, BN1 9QH, UK*

²*Astrophysics Research Centre, Queen's University, Belfast, County Antrim, BT7 1NN, UK*

Accepted Received; in original form 2011 August 19

ABSTRACT

We present Roche tomograms of the secondary star in the dwarf nova system RU Pegasi derived from blue and red arm ISIS data taken on the 4.2-m William Herschel Telescope. We have applied the *entropy landscape* technique to determine the system parameters and obtained component masses of $M_1 = 1.06 M_\odot$, $M_2 = 0.96 M_\odot$, an orbital inclination angle of $i = 43^\circ$, and an optimal systemic velocity of $\gamma = 7 \text{ km s}^{-1}$. These are in good agreement with previously published values.

Our Roche tomograms of the secondary star show prominent irradiation of the inner Lagrangian point due to illumination by the disc and/or bright spot, which may have been enhanced as RU Peg was in outburst at the time of our observations. We find that this irradiation pattern is axi-symmetric and confined to regions of the star which have a direct view of the accretion regions. This is in contrast to previous attempts to map RU Peg which suggested that the irradiation pattern was non-symmetric and extended beyond the terminator.

We also detect additional inhomogeneities in the surface distribution of stellar atomic absorption that we ascribe to the presence of a large star-spot. This spot is centred at a latitude of $\sim 82^\circ$ and covers approximately 4 per cent of the total surface area of the secondary. In keeping with the high latitude spots mapped on the cataclysmic variables AE Aqr and BV Cen, the spot on RU Peg also appears slightly shifted towards the trailing hemisphere of the star. Finally, we speculate that early mapping attempts which indicated non-symmetric irradiation patterns which extended beyond the terminator of CV donors could possibly be explained by a superposition of symmetric heating and a large spot.

Key words: stars: novae, cataclysmic variables – stars: starspots – stars: late-type – stars: imaging – stars: individual: RU Peg – techniques: spectroscopic

1 INTRODUCTION

Cataclysmic variables (CVs – see Warner (1995) for an excellent review) are a class of interacting binary characterised by a white dwarf star, known as the primary, accreting material via an accretion disc or column from the secondary – typically a late-type main-sequence dwarf star. CVs are often studied in order to gain insight into the processes of astrophysical accretion, but it is the secondary star that holds the key to unlocking our understanding of the creation and evolution of these systems and their corresponding behaviour. In the canonical scenario for the evolution of CVs, for example, the magnetic field of the secondary star is believed

to play a crucial role in draining away angular momentum from the system via a process known as *magnetic braking* (see, e.g., Kraft (1967), Mestel (1968) and Spruit & Ritter (1983)). This is thought to be responsible for maintaining mass transfer and for causing long period CVs to evolve to shorter orbital periods. At orbital periods of about 3 hours and stellar masses of around $0.25 M_\odot$, the secondary star is thought to become fully convective. Under the canonical theory of CV evolution, this transition to a fully convective interior switches off the stellar dynamo and consequently mass transfer is quenched. Contact with the inner Lagrangian point is re-established at shorter periods through removal of angular momentum via gravitational radiation. This explains the so-called *period gap* in the period distribution of the total CV population. Despite the acceptance of this model, there is little or no direct observational evidence for such an abrupt change in the angular momentum loss

* E-mail: alexander.dunford@gmail.com

† E-mail: c.a.watson@qub.ac.uk

‡ E-mail: r.c.smith@sussex.ac.uk

mechanism and it is still unclear whether magnetic braking is really the dominant loss mechanism above the period gap. Magnetic activity cycles have also been cited as possible causes for a number of other observed CV phenomena, such as variations in orbital periods, luminosity, mean outburst durations and outburst shapes (e.g. Applegate (1992), Richman et al. (1994) and Ak et al. (2001)). Given the importance of understanding the underlying magnetic properties of these stars, it is therefore highly desirable to try to obtain observational evidence for such fields, in the form of the sizes, distributions and lifetimes of star-spots.

In addition, since CV secondaries are among the fastest rotating set of stars known, we may begin to use them as natural laboratories to provide tests of stellar dynamo theory, since they should display strong dynamo action. We may also begin to ask what effect tidal forces have on the emergence of magnetic flux tubes. It has been suggested that tidal forces may suppress differential rotation (Scharlemann 1982) and force star-spots to form at preferred longitudes (Holzwarth & Schüssler 2003). Since CV secondaries are heavily tidally distorted, it seems clear that these systems are perfect for probing these effects.

However, despite the clear importance of magnetic behaviour in the evolution of CVs and the potential gains to be had in our understanding of the so-called solar-stellar connection, until recently there has been little work undertaken in this field. Webb et al. (2002) used TiO bands to determine a spot coverage factor of 22 per cent for the secondary in SS Cyg, although their work did not actually map the surface. Recently, however, the technique of Roche tomography has begun to allow the mapping of the surface of these stars, and results presented in papers III and IV of this series have reported the first detection of star-spots on a CV secondary (AE Aqr – Watson et al. 2006) followed by a similar mapping campaign for BV Cen (Watson et al. 2007a). Both maps showed spots at almost all latitudes, as well as large near-polar spots similar to those found in Doppler imaging studies of single stars. In this work, we report on attempts to apply this technique to the dwarf nova RU Peg for the first time. RU Peg is a relatively bright ($m_v=13.1$ rising to 9.5 during outburst) U Geminorum type dwarf nova with an orbital period of 9 hours.

2 OBSERVATIONS AND DATA REDUCTION

2.1 Observations

Observations of RU Pegasi were made with the 4.2-m William Herschel Telescope (WHT) at the Roque de los Muchachos Observatory on the island of La Palma over the nights of 20–23 July 2004. A journal of these observations can be found in Table 1. The ISIS double beam spectrograph, which makes use of a dichroic mirror to split the incoming light into blue and red channels, was used to obtain simultaneous blue and red spectra. The central wavelengths for the blue and red spectra were selected to be 4950Å and 6400Å respectively, yielding unvignetted ranges of 4550–5350Å in the blue and 6070–6700Å in the red. Both arms of ISIS made use of the R1200 gratings giving a dispersion of about 0.23Å/pixel. A two-pixel resolution of about 28 km s⁻¹ in the blue and 22 km s⁻¹ in the red was obtained

for a slit width of 1 arcsec. Exposure times were selected in such a way as to balance the requirement for maximum signal while remaining short enough to avoid the effects of velocity smearing. Observations of the flux standard star SP 2148+248 were taken at or close to the zenith, in order to correct for the instrumental response and to remove any telluric absorption features in the red data.

Since we require good relative flux calibration, we placed the nearby comparison star RU Peg Ref 2 (Harrison et al. 2004) on the slit to allow for slit-loss corrections and any variations in sky transparency. In addition to a number of observations of K and M spectral-type templates, arc spectra were taken before and after each exposure (or multiple run of six ten minute exposures in the case of RU Peg) to enable the spectra to be wavelength calibrated and to correct for any flexing in the instrument as the telescope tracks the target. A set of tungsten flat fields and bias frames was also taken at the beginning and end of each night. The weather during the observing run varied from clear to heavy rain and fog. In effect, this resulted in the loss of one night out of four. Mechanical breakdowns also restricted the amount of observing we were able to accomplish. Amateur V band photometric observations (obtained by Roger Pickard and Gary Poyner of the British Astronomical Association Variable Star Section (BAA VSS), whom we gratefully acknowledge) showed that the system was not in quiescence during our observations. Rather, it was on the rise to peak outburst luminosity. The average blue and red arm spectra can be seen in Fig. 1.

2.2 Data reduction

The raw images were bias-subtracted using a median bias value obtained from the overscan region. Pixel-to-pixel variations were removed by creating a master balance frame, generated from a set of tungsten flats, and dividing each raw frame through by the master balance frame. The spectra were finally sky subtracted and optimally extracted (Horne 1986) using the software package PAMELA. The Copper Argon/Copper Neon (CuAr+CuNe) arc spectra were also optimally extracted, from the same region of the chip that the object spectrum occupied. These were fitted with a fourth order polynomial giving an rms scatter of better than 0.001Å. The object spectra were then placed on this wavelength scale. The data were then flux calibrated using spectra of the featureless white dwarf star SP 2148+286.

Roche tomography also requires that we correct for slit-losses and variable sky transmission. This is due to the rapidly varying and unknown spectral contribution of the accretion disc. Because ISIS is not a cross-dispersed spectrograph, and so is capable of long-slit spectroscopy, we were able to place a non-varying comparison star (RU Peg Ref 2; Harrison et al. 2004) on the slit and take wide and narrow slit exposures. We then multiplied each corresponding CV spectrum by the ratio of the wide slit comparison spectrum to the narrow slit comparison spectrum. We should note that since the slit was not set to follow the parallactic angle, this is at the expense of some small effects arising from differential refraction. Since we treat both the red and blue arms independently during the Roche tomography reconstructions later, this reduces our exposure to such effects.

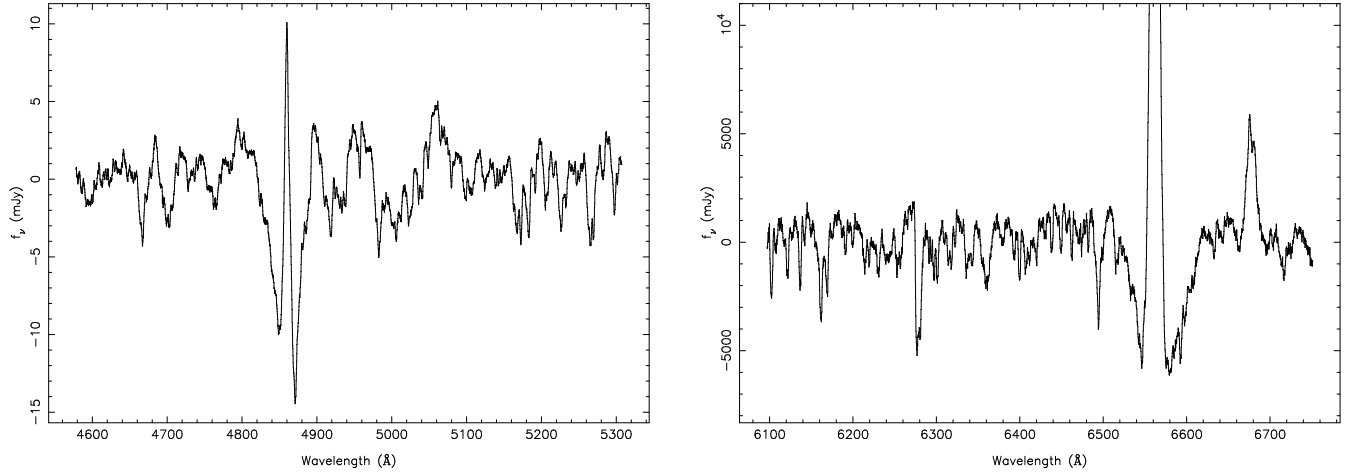


Figure 1. *Left* – WHT+ISIS average blue arm spectrum of RU Pegasi. *Right* – WHT+ISIS average red arm spectrum of RU Pegasi. In both cases the orbital motion of the secondary star has been removed prior to co-adding, and the continuum has been subtracted.

Object	Date	UT Start	UT End	T_{exp} (s)	No. of spectra	Comments
BD+03 3568	2004 July-20	23:08	23:23	300	2	G8V template
BD+05 3625		23:25	23:35	600	1	K0V template
GAT 746		23:52	00:02	600	1	K1V template
RU Peg		00:22	02:11	600	13	CV target
SP 2148+286	2004 July-21	02:42	02:52	600	1	Spectrophotometric standard
SP 2148+286		02:53	03:03	600	1	Spectrophotometric standard wide slit
RU Peg		03:15	05:32	600	13	CV target
HD 154363		21:53	21:55	120	1	K5V template
HD 181196	2004 July-22	22:03	22:05	180	1	K5V template
HD 332601		22:09	22:14	600	1	K5V template
HD 160964		22:24	22:28	240	1	K4V template
SP 2148+286		00:34	00:44	600	1	Spectrophotometric standard
SP 2148+286	2004 July-23	00:45	01:06	600	2	Spectrophotometric standard wide slit
RU Peg		01:28	05:41	600	45	CV target
BD+00 3459		22:49	22:50	60	1	K3V template
RU Peg		02:35	04:37	600	22	CV target
BD+30 3627	2004 July-23	04:47	04:52	300	1	K2V template
SP 2148+286		04:56	05:06	600	1	Spectrophotometric standard
HD 333388		05:14	05:16	150	1	K8V template
BD+01 3236		21:39	21:47	450	1	K7V template
GJ 9606	2004 July-23	22:10	22:20	600	1	M0V template
GJ 9645		22:27	22:35	450	1	K6V template
SP 2148+286		22:41	23:15	600	3	Spectrophotometric standard
RU Peg		02:26	03:48	600	13	CV target

Table 1. Journal of observations for the July 2004 WHT/ISIS run. The first column gives the object name, followed by the date and start/end times of the observations. The final three columns indicate the exposure times (for the blue arm of ISIS), the number of spectra obtained and an indication of the type of spectra taken.

3 THE SECONDARY STAR

3.1 Projected rotational velocity

In order for accurate orbital phases to be calculated for our spectra, a new orbital ephemeris was required (see section 3.2). However, in order to provide the most accurate cross-correlation between our target spectra and the template, we also need an estimate for the mean line width of the target spectrum. To be able to measure the mean projected equatorial rotational velocity of the secondary, $v \sin i$, we require an average spectrum for maximum signal to noise. Simply creating a mean spectrum at this point would be fu-

tile, as the orbital motion of the secondary would effectively smear out the absorption line profiles due to the Doppler shifts throughout the orbit. We therefore subtracted the radial velocity of each spectrum individually, having determined their velocities through cross-correlation with a high signal-to-noise spectral-type template star. The spectra are, of course, composites of all the components in the CV. To ensure the secondary star line strengths were preserved across the region of interest, the spectra were first rebinned onto the same velocity scale using sinc-function interpolation and then normalised by dividing through by a constant. Finally, the spectral continua were fitted with a third-order spline

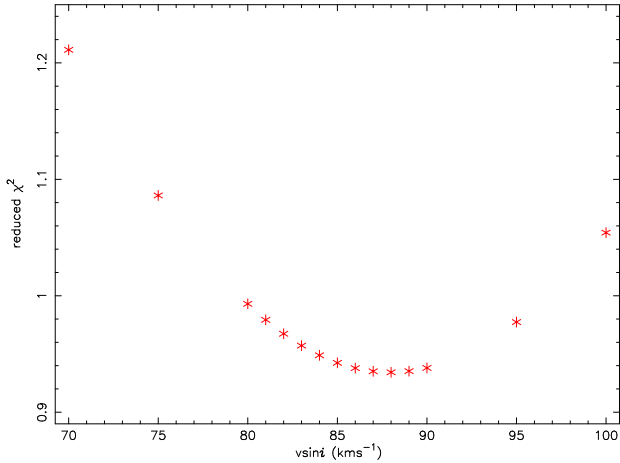


Figure 2. χ^2 versus $v \sin i$ obtained through cross correlation with a K5V template. The minimum is located at a projected rotational velocity of 88 km s^{-1} . Note (see text) that the broadening increment of 5 km s^{-1} has been reduced to 1 km s^{-1} around the minimum to allow its position to be better determined.

which was then subtracted. An identical procedure was applied to the spectral type template with the added complication that the spectral type standard was corrected for its systemic velocity.

The majority of our template stars do not have prior systemic velocity measurements and so we used Least Squares Deconvolution (LSD – see section 4) to calculate a mean absorption line profile for each spectrum. This mean profile was then fitted with a gaussian and the location of the peak of the fit was taken as the template’s radial velocity. Table 2 lists the measured radial velocities of our spectral type templates. A previous estimate of the radial velocity of our K5V template GL 653 can be found in Evans (1967) who reported a value of $33.6 \pm 2 \text{ km s}^{-1}$. This is within 1.5σ of our LSD derived estimate of 30.6 km s^{-1} .

A first iteration on the radial velocity curve was obtained by cross-correlating the RU Peg spectra with a K5V template that had been rotationally broadened by an arbitrary amount, 100 km s^{-1} in this instance. We used the red arm data, specifically wavelengths between 6200 \AA & 6500 \AA , since this range contains a number of relatively strong stellar absorption lines and also some known temperature and gravity sensitive lines for K type stars (Strassmeier & Fekel 1990). This first pass made it possible to subtract approximate radial velocities of the spectra and create an average RU Peg spectrum.

The template spectrum was then artificially broadened by 5 km s^{-1} increments, multiplied by some constant and then optimally subtracted from the average RU Peg spectrum. In this process, the fraction of the template that best removes the secondary star lines is calculated using an optimisation technique that minimises the scatter between the template and the target in a process known as *optimal subtraction* (a term first used by Dhillon & Marsh (1993) and widely used since in the context of secondary stars in CVs). Fig. 2 shows the results of this method for the K5V template, where we have decreased the broadening increment to 1 km s^{-1} around the curve’s minimum. The optimum value of $v \sin i$ is 88 km s^{-1} .

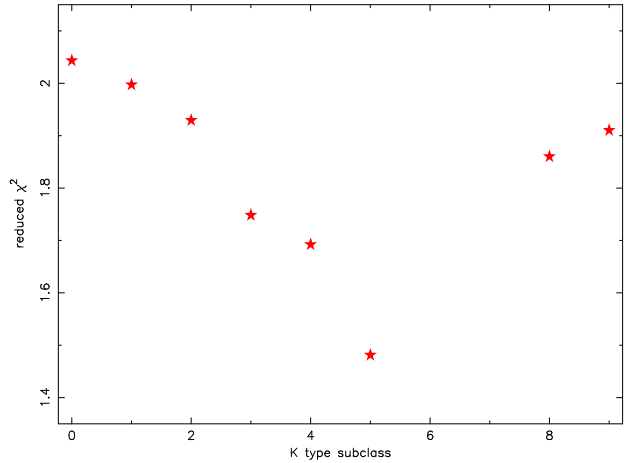


Figure 3. RU Peg secondary star spectral type. The x -axis refers to the subclass of K dwarf template used in the optimal subtraction procedure described in section 3.1.

To test whether our choice of spectral type template introduces systematic errors, or indeed if there is any trend in the measured value of $v \sin i$ with spectral type, the procedure has been repeated for all our spectral type templates. We find that the choice of spectral type does not significantly affect the resulting optimal value for $v \sin i$ – the standard error on the mean of our sample is only 0.5 km s^{-1} . In each application of artificial broadening, we have assumed a simple linear limb darkening law with a coefficient of 0.5,

$$\frac{I(\mu)}{I(0)} = 1 - a(1 - \mu) \quad (1)$$

where $\mu = \cos \delta$ (δ being the angle between the line of sight and the emerging intensity), $I(0)$ is the specific intensity at the centre of the stellar disc and a is the linear limb darkening coefficient (see Claret 1998). Again, to test for the possibility of introducing systematic errors, the entire procedure has been run using a range of values from 0 to 1 for the limb darkening coefficient. The optimum values of $v \sin i$ did not differ from each other by more than 3 km s^{-1} . We therefore adopt $v \sin i = 88 \pm 3 \text{ km s}^{-1}$.

The spectral type of the secondary star can also be estimated using optimal subtraction, given a full set of spectral type templates. Fig. 3 shows the reduced χ^2 against K dwarf subtype which displays a minimum at K5V. Again, we tested the effect limb darkening has on the outcome. We found no change in the optimum spectral type while varying the linear limb darkening coefficient. Our estimated spectral-type compares well with the previous estimated spectral type of K3V adopted by Friend et al. (1990) following the work of Wade (1982).

3.2 Radial velocity curve and ephemeris

The most recent orbital ephemeris for RU Peg was derived from secondary star radial velocity variations by Friend et al. (1990). Given the long gap between their observations and the ones reported here, a large error may have accumulated in the orbital zero point. We have derived a new ephemeris by cross-correlating our red arm RU Peg data with the best-fitting K5V spectral type template GL 653 to

produce a series of cross-correlation functions (CCFs). The RU Peg and the GL 653 spectra are treated in the same way as described in section 3.1, with the template being artificially broadened by the optimum amount found through optimal subtraction, in this case 88 km s^{-1} . In addition, the radial velocity of the K5V template has been removed. A cross correlation function was generated for each RU Peg spectrum, and the radial velocity curve obtained by fitting a sinusoid through the CCF peaks. The following ephemeris:

$$T_0 = 2453207.53376 \pm 0.00009, \quad (2)$$

was obtained where the orbital period has been fixed at 0.3746 days (Stover 1981), and T_0 is the time of inferior conjunction of the secondary star, in the heliocentric reference frame. The quoted uncertainty is statistical, with no allowance for any possible systematic effects. This new zero point has been used in all subsequent analysis. The robustness of this method of generating a radial velocity curve through cross-correlation against an incorrect template choice has been tested. A series of CCFs was produced using the full range of K dwarf templates at our disposal, and it was found that, providing the templates were correctly broadened, there was no significant change in the value of the semi-amplitude or systemic velocity, and therefore the zero-crossing.

In Fig. 4, the radial velocity points have been assigned an orbital phase based on the new ephemeris, and fitted with a circular fit of the form,

$$V(\phi) = \gamma + K_2 \sin \frac{2\pi(t - t_0)}{P_{\text{orb}}}, \quad (3)$$

where K_2 is the semi-amplitude of the secondary star, γ is the systemic velocity, $V(\phi)$ is the radial velocity at a phase ϕ , t is the time of observation, t_0 is the zero crossing and P_{orb} is the orbital period. From this fit we obtain a value for the radial velocity semi-amplitude of $128.2 \pm 0.6 \text{ km s}^{-1}$. This compares with a value of $111 \pm 8 \text{ km s}^{-1}$ found in Kiplinger (1979), $121 \pm 2 \text{ km s}^{-1}$ from Stover (1981) and $121 \pm 2 \text{ km s}^{-1}$ derived in Friend et al. (1990). We should add at this point that there is a clear systematic trend in the residuals of the circular fit of Fig. 4. This is most likely the result of irradiation, making such conventional studies susceptible to systematic errors since the centre-of-light of the secondary no longer represents its centre-of-mass. Our value for the systemic velocity of $10 \pm 0.5 \text{ km s}^{-1}$ compares well with Friend et al. (1990) who report a value of $13 \pm 2 \text{ km s}^{-1}$, and Stover's value of $5 \pm 4 \text{ km s}^{-1}$. The analysis of Kiplinger (1979) yielded a slightly more discrepant value of $-1 \pm 5 \text{ km s}^{-1}$ using the radial velocity data obtained in Kraft (1962), though the value changes to $18 \pm 6 \text{ km s}^{-1}$ when measuring γ from a disc emission line radial velocity curve.

Additional motivation for measuring the projected rotational velocity and K_2 is that one can determine a value for the mass ratio and in turn, the semi-amplitude of the primary star. From Horne et al. (1986), the predicted rotational velocity for a Roche-lobe filling star is given by:

$$v \sin i = \frac{R_L}{a} K_2 (1 + q). \quad (4)$$

Combining this with the approximation of Smith & Dhillon (1998) for the volume-averaged Roche lobe radius (assumed

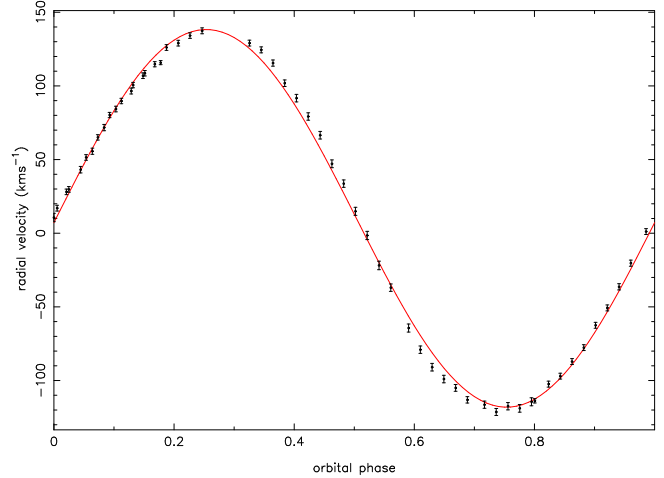


Figure 4. RU Peg (ISIS red arm) radial velocity data (filled circles) and circular orbital fit.

equal to the radius of the secondary star) gives the following relation:

$$v \sin i = 0.47 K_2 q^{1/3} (1 + q)^{2/3}. \quad (5)$$

Rearranging for q , the mass ratio (defined as M_2/M_1), and inserting our values for $v \sin i$ and K_2 derived earlier, equation (5) can be solved to obtain $q = 0.88 \pm 0.02$. This is higher than the values of 0.78 and 0.79 found in Stover (1981) and Kiplinger (1979), both obtained directly through measurements of both K_1 and K_2 . Given the relatively poor quality of their emission line radial velocity curves, it may be argued that the value derived here from accurate rotational velocity measurements is somewhat more reliable, although our value for K_2 has not fully taken into account the residuals in the fit. Friend et al. (1990) derive a value of $q = 0.82 \pm 0.15$ from their rotational broadening measurements that is slightly closer to ours. However, the value presented here is considered an improvement given the higher resolution of our data. Our mass ratio and K_2 imply a primary star radial velocity semi-amplitude $K_1 = 112.6 \pm 0.25 \text{ km s}^{-1}$. Kiplinger (1979) reports a value of $88 \pm 10 \text{ km s}^{-1}$, significantly lower than our value, from direct measurement of the H α emission wings; although the fit is reasonable, the reported rms error is 26 km s^{-1} . Stover (1981), using a similar method for measuring the emission wing velocities, finds a value of $94 \pm 3 \text{ km s}^{-1}$ fitting a circular orbit to the radial velocity data (with an rms error of 12 km s^{-1}). We note here that no attempt has been made to directly measure the emission line radial velocities in this work due to the complicated nature of the emission line profiles. Since the system is in outburst, we see that H β and H α have two anti-phased components – one from the disc and one from the irradiated surface of the secondary.

4 LEAST SQUARES DECONVOLUTION

While single absorption-line studies of CV donor stars using intermediate resolution spectrographs on 4-m class telescopes have been successful in mapping large-scale irradiation patterns on their surfaces (e.g. Watson et al.

Spectral Type	Name	Radial Velocity (km s ⁻¹)
G8V	BD+03 3568	-0.3
K0V	BD+05 3625	-31.9
K1V	GAT 746	-50.0
K2V	BD+30 3627	-57.3
K3V	BD+00 3459	-5.3
K4V	HD 160964	-20.8
K5V	GL 653	30.6
K8V	HD 333388	-7.1

Table 2. Heliocentric radial velocities of spectral type templates measured via a Gaussian fit to the mean profile.

2003), they have not been successful at mapping star-spots because of the limited resolution and signal-to-noise of such data. Watson et al. (2006), however, applied the technique of Least Squares Deconvolution (LSD – Donati & Collier Cameron 1997) to produce a mean profile by combining several thousand absorption lines from the secondary star in AE Aqr observed with the UES echelle spectrograph on the WHT. This achieved the required signal-to-noise to observe the effects of star-spots on the line profile.

LSD requires the positions and strengths of the atomic absorption lines present in the stellar spectrum to be known. In this work, we use an atomic line list generated by the Vienna Atomic Line Database (VALD, Kupka et al. (1999, 2000)). VALD offers a simple online interface for the selection of the required data; all that is required are values for the stellar effective temperature and surface gravity, the relevant wavelength range, micro-turbulence (due to small scale motions of convective cells at the stellar surface, taken here to be $\approx 1 \text{ km s}^{-1}$) and a detection limit for the strengths of the normalised lines. The detection limit in Doppler imaging applications is often taken to be about 0.4 (this is the lower limit to the central line depth, ignoring line blending and expressed as a fraction of the continuum). Since we are dealing with intermediate resolution data rather than echelle data, we have used a more conservative 0.5 (this may still seem optimistic; however tests described below indicate that the input line list has little effect on the shape of the mean profile). The spectral type of RU Peg has been estimated in this work as K5V – the closest model available in the VALD database corresponds to a stellar atmosphere with an effective temperature, T_{eff} , of 4600K and $\log(g/\text{cm s}^{-2}) = 4.6$.

The composite nature of the CV spectrum complicates the situation with regard to treating the spectral continuum. There is a varying and unknown contribution from the accretion regions, as well as a changing continuum slope due to any time variability and the changing sky projection of the accretion disc and hot spot. This means that the creation of a master continuum fit (e.g. Collier-Cameron & Unruh 1994) is impossible and we are forced to remove the continuum on a spectrum by spectrum basis. Simply normalising the spectra is also inappropriate, as the varying secondary star contribution would result in the relative line strength changing from one spectrum to the next. We therefore continuum subtracted the data (after flux calibration and slit-loss correction) by subtracting a smoothly varying fit for each spectrum. This fit is created by placing spline knots at positions that are relatively free of absorption lines, while simultaneously ignoring strong disc emission lines.

This method of fitting the continuum may appear rather subjective, since it is often difficult to decide exactly how the continuum varies across a spectrum. Tests were carried out to determine the effects of incorrect continuum fits on the final mean profile by constructing two continuum fits to the same spectrum – the first being our best guess at the true continuum and the second was a fit which was clearly wrong. We find that the continuum fit does not have a significant effect on the *shape* of the resultant mean profile. However the continuum fit chosen does, of course, have an impact on the level of the continuum seen in the mean profiles. In general, it was found that the final continuum fit selected was at too high a level, resulting in the (subtracted) continuum wings of the mean profiles lying well below zero. This is straightforward to remedy by iteratively lowering the level of the continuum fit until the desired zero continuum level is achieved in the LSD profile. Again, this process was found not to alter the shape of the mean profile.

It should be noted that since our line list contains normalised line depths and our spectroscopic data are continuum subtracted, a further step was needed to prepare the line list for use with our data. Each line depth in the line list was multiplied by the value of a continuum fit to a K5V spectral type template at that wavelength. In this way, the line list now contains a set of lines that have the correct relative depths and may be used with continuum subtracted data. The sensitivity of the LSD process to the choice of line list used has been investigated by carrying out LSD on the same RU Peg spectrum using a range of spectral type line lists that covers the spectral types K0V to K8V inclusive. As in Barnes (1999), there is no evidence that slight errors in the assumed spectral type, and therefore an incorrect line list, introduces any appreciable systematic errors in the final average profile.

5 ROCHE TOMOGRAPHY

Roche tomography is an astro-tomographic technique developed to image the surface of the secondary star in cataclysmic variables (Rutten & Dhillon 1994; Watson 2002). The procedure is, by now, robustly tested and artefacts caused by systematic errors are well understood (see Watson & Dhillon 2001 for details). Early work focused on mapping single absorption or emission lines (see Watson et al. 2003) while, more recently, efforts have been made to map star-spot patterns (see Watson et al. 2006, 2007a).

Roche tomography takes as its input a trail of phase resolved spectral line profiles, and produces a map of the secondary star in three-dimensional real space. The key advantage this technique has over other indirect imaging methods (such as Doppler tomography) is that it makes use of all the information contained in the line (i.e. its flux, width and Doppler shift) to map the star. Roche tomography is, however, very similar to Doppler imaging of single stars, but for the exceptions that in Roche tomography the star is Roche-lobe filling, rotates around the binary centre-of-mass, and is tidally locked. Roche tomography also ignores the continuum. Successfully applying the technique is often somewhat harder than Doppler imaging. Roche tomography targets are generally much fainter than the targets of choice in single

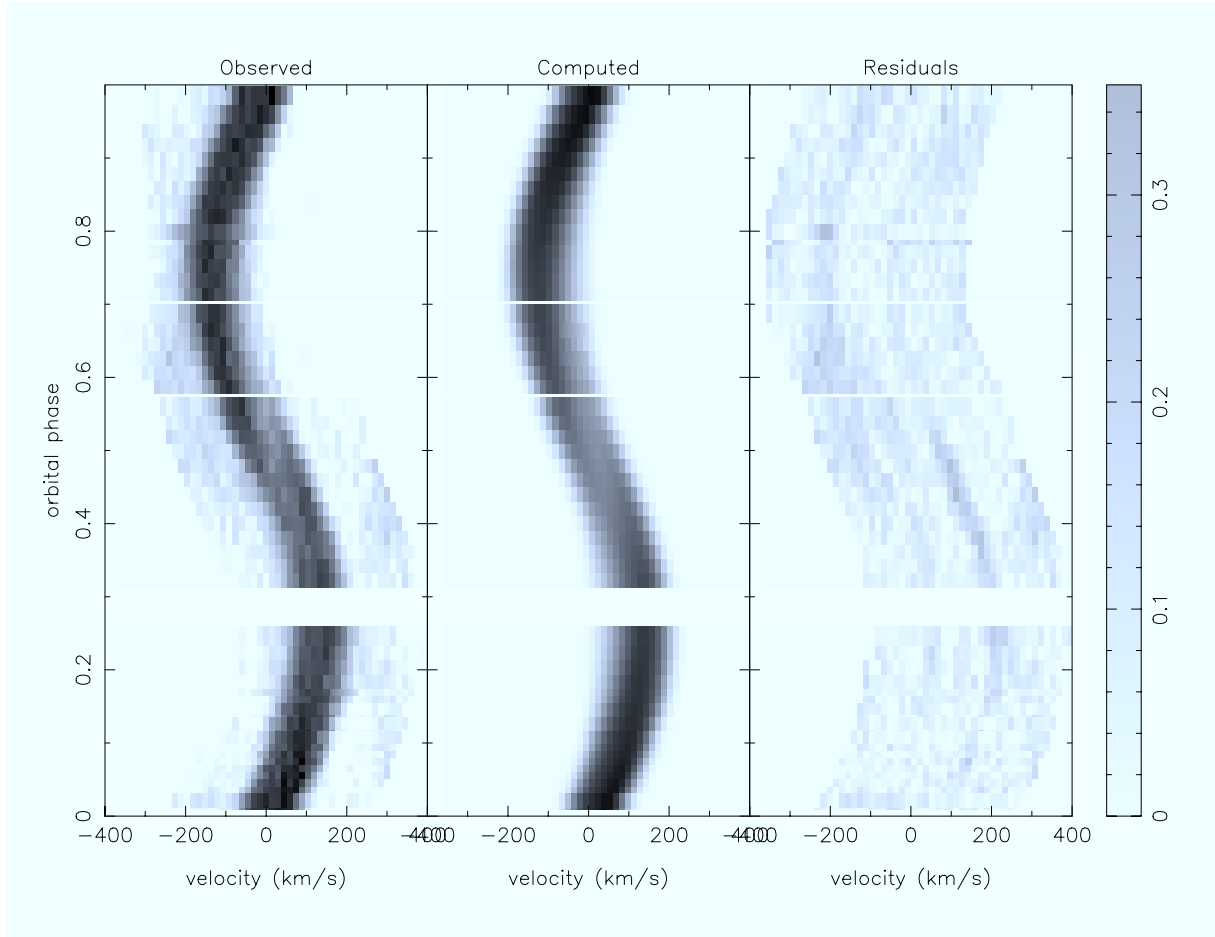


Figure 5. Roche input trailed spectrum, computed data and residuals for RU Peg blue data. Dark grey scales depict deeper line depths relative to lighter grey scales.

star mapping programs, resulting in spectral profiles of lower signal-to-noise and poorer quality maps.

We use the tomography code *Roche* developed by Watson (2002) and first applied with the addition of LSD by Watson et al. (2006). The synthetic LSD profiles were constructed by assuming that each tile contributes a Gaussian profile to each line, scaled by projected area and intensity. Although temperature and abundance will affect the profile, so that the spot contribution to the profile will be slightly different from one line to another, we don't have enough information to take that into account and we simply compute an average profile for each tile, and use that average profile in the mapping. The LSD process is not very sensitive to temperature and metallicity effects (Barnes 1999). Although for single stars it is possible to assume for each tile some combination of 'spot' and 'immaculate' assumed spectrum, that is not possible here because irradiation means that there is no single 'immaculate' spectrum – and indeed the contribution of irradiation is something that we want to obtain. We recognise that this means that what the *Roche* code produces is essentially a contrast map.

5.1 System parameters

The use of incorrect system parameters in the Roche tomography reconstruction results in artefacts being mapped onto the stellar grid (Watson & Dhillon 2001). For example, a set of incorrect values for the masses and the orbital inclination will result in the code not being able to properly fit the variations of the profile widths along the trail. Roche tomography allows a natural method of selecting optimal values for these parameters, since only the correct values will give the map of maximum entropy. We carry out reconstructions for a set of component mass pairs, fitting to the same χ^2 each time, until a full grid of values is obtained – the so-called entropy landscape (Rutten & Dhillon 1994).

Limb Darkening

An incorrect treatment of the limb darkening for the secondary star may also result in extra structure being mapped onto its surface. In this work we make use of a square-root limb darkening law of the following form (Claret 1998),

$$I(\mu) = I_0 [1 - a_\lambda (1 - \mu) - b_\lambda (1 - \sqrt{\mu})], \quad (6)$$

where a_λ and b_λ are the limb darkening coefficients at a wavelength λ . Claret (1998) emphasises the non-linearity of limb darkening laws applied to model atmospheres of late K

and M type main sequence stars; for the coolest stars, the departure from linearity is drastic.

Since limb darkening is a function of wavelength, we determine an effective central wavelength for the blue arm ISIS data of 4875\AA that takes into account the line depths and spectral noise and is calculated after Watson et al. (2006) using,

$$\lambda_{\text{cen}} = \frac{\sum_i (1/\sigma_i^2) d_i \lambda_i}{\sum_i (1/\sigma_i^2) d_i}, \quad (7)$$

where d_i and σ_i are the flux and error at wavelength λ_i , respectively.

We assume a secondary star spectral type of K5V (see section 3.1) and adopt values for the effective temperature of 4557K and log surface gravity (in cm s^{-2}) of 4.6 (Gray 1992). The closest model available in the database of non-linear limb darkening coefficients provided by Claret (1998) has an effective temperature of 4660K and surface gravity of 4.6 . We obtained values for the limb darkening coefficients in the Johnson B and V bands and linearly interpolated across them to arrive at values corresponding to the calculated effective central wavelength of our spectra. These coefficients, $a_\lambda = 0.8062$ and $b_\lambda = 0.0538$, are used in all subsequent reconstructions. For the red arm ISIS data with an effective central wavelength of 6426\AA , we obtain coefficients of $a_\lambda = 0.482$ and $b_\lambda = 0.347$ for the Johnson R band ($\lambda_{\text{cen}} = 6300\text{\AA}$). Note that it was not possible to interpolate values of the coefficients at our central red wavelength, because of a lack of limb darkening data for photometric bands later than R in Claret (1998).

Note that we have used continuum limb-darkening coefficients. We recognise that coefficients for the cores of absorption lines are considerably smaller; however, the precise values for line limb-darkening coefficients depend on many factors, such as the angle of incidence, and therefore require detailed and time-consuming calculations (e.g. Collins II & Truax (1995)). We have not attempted these, for three reasons. Firstly, it is the wings of the lines, where the difference from the continuum is least, that constrain the rotation and therefore the mass ratio. Secondly, we have tried varying the limb-darkening coefficients, and even with no limb darkening the maps still show the same gross features, although the parameters change slightly. Thirdly, the coefficients we have chosen give a somewhat lower χ^2 than other values we tried, even though the results are not very sensitive to the choice.

Systemic velocity, inclination and component masses

Figs 6(a) and (b) show surfaces of maximum entropy for a set of inclinations and systemic velocities for the blue and red ISIS data, respectively. For each systemic velocity/inclination pair an entropy landscape has been constructed, and the maximum entropy value extracted. In practice, an inclination value is first selected based on previous estimates and a series of entropy landscapes are generated for a range of systemic velocities.

Previous Roche tomography work (Watson et al. 2003, 2006, 2007a) has shown that for almost any choice of inclination (and indeed for a wide range of mass pairs) the entropy landscape yields the same systemic velocity. This is

also true here, where for the blue data, the optimum systemic velocity of 7 km s^{-1} is constant for the range of inclinations probed. Fig. 6(c) shows a slice through the entropy surface shown in Fig. 6(a) at an inclination of 43° , showing a peak in the entropy at 7 km s^{-1} . Similarly, Fig. 6(d) shows a cut through the red maximum entropy surface at an inclination of 42° , where the entropy clearly peaks at a systemic velocity of 6.5 km s^{-1} . It is comforting to note that the optimal systemic velocity derived from two essentially independent data sets is constant for the full range of inclinations probed, and has essentially the same value for the two data sets.

We are unable to assign a fully rigorous (Monte Carlo) error determination as such a procedure would be vastly computationally expensive (see also below). Test reconstructions, using values for the systemic velocity on either side of our optimum value, result in rapid degradation of the image quality, as also found by Watson et al. (2007a), who reported that “reconstructions were almost impossible for assumed systemic velocities that differed by more than $\pm 2\text{ km s}^{-1}$ from the optimal value”. In addition, we found that viable reconstructions are impossible at inclination values $\pm 10^\circ$ from our optimum value. It is therefore unlikely that the errors exceed half these extreme values.

While our optimal systemic velocity is close to the value derived from the more traditional radial velocity study in Section 3, which yielded $10.2 \pm 0.4\text{ km s}^{-1}$ for the systemic velocity, it does not agree with it within the error bars. This is not too surprising, since the value obtained through the radial velocity curve is subject to an incomplete treatment of the surface distribution of flux on the secondary, which is known to cause systematic errors in the systemic velocity determination. Indeed, as noted earlier, there remain residual radial velocities of up to $\sim 10\%$ at some orbital phases after fitting a circular orbit to the radial velocity data.

Kiplinger (1979) used the earlier radial velocity data of Kraft (1962) to derive a value of $-1 \pm 5\text{ km s}^{-1}$ for the systemic velocity (though he was unable to detect the secondary star in this work due to severe veiling of the secondary lines by a bright disc on decline from outburst). It should be noted that the work of Kraft (1962) represents the earliest detection of RU Peg as a binary, and the radial velocity data reported there are derived from very low resolution data, with the subsequent orbital fit showing a large scatter. Our value is consistent with Stover (1981), who reports a systemic velocity of $5 \pm 4\text{ km s}^{-1}$ derived from observations of the system taken in quiescence with higher quality data. Friend et al. (1990) quote a slightly larger value of $13 \pm 2\text{ km s}^{-1}$ using the NaI doublet, though they question whether or not the secondary star semi-amplitude is truly accurate, or if it is biased by low level irradiation. It is noted here that an accurate value for the radial velocity of the template used in the cross-correlation is also important, since this must be subtracted from the CV radial velocity data prior to orbital fitting. In our case, this has been accurately measured using LSD.

Once the systemic velocity has been determined, it is then possible for the inclination and the component masses to be determined. These are solved for essentially simultaneously, although for computational convenience we in practice chose a value of i and produced an entropy landscape for the two masses, then repeated this process for a range

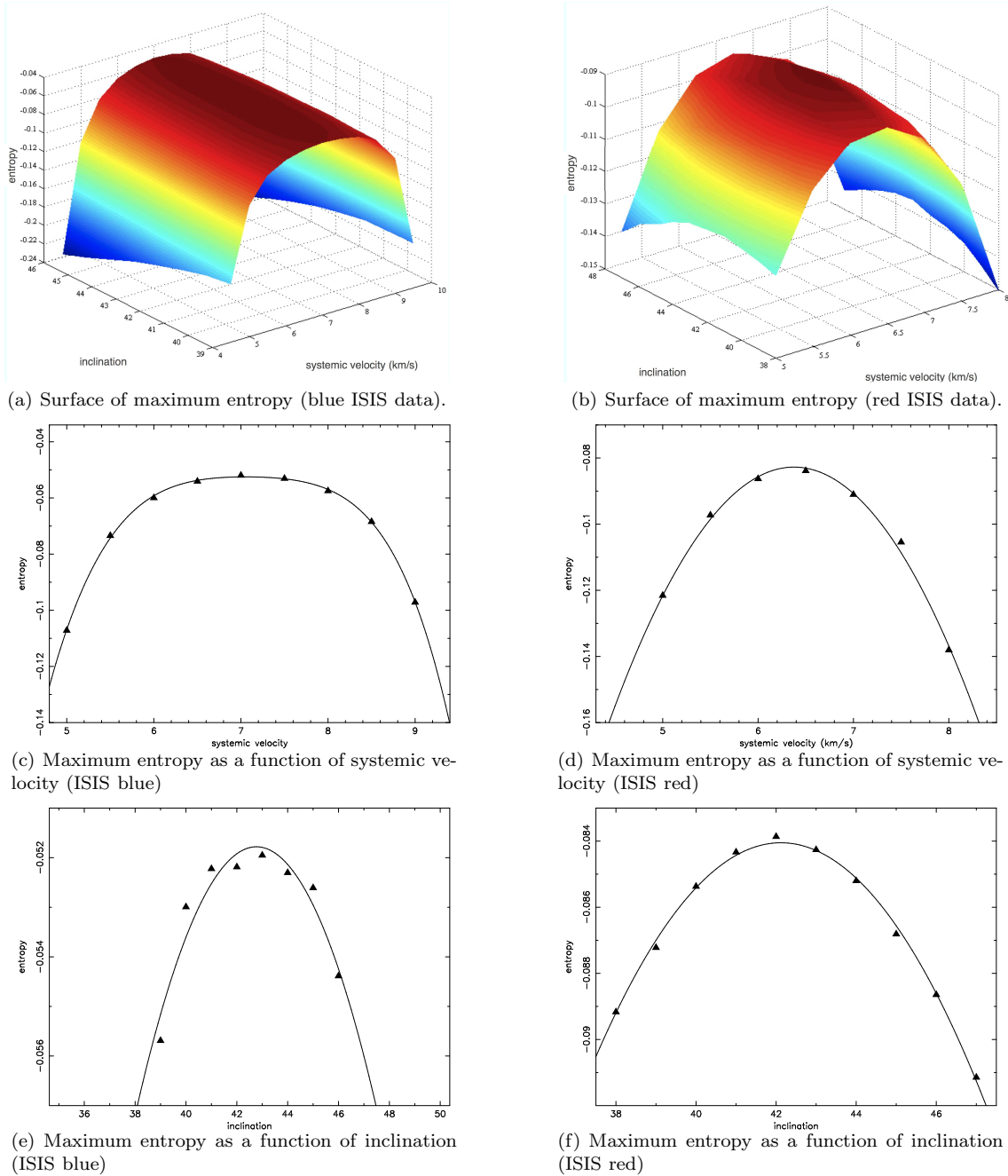


Figure 6. Optimal system parameters. In the top panels, the value of each point on the surface is obtained from an entropy landscape carried out at a particular combination of orbital inclination and systemic velocity. The optimum systemic velocity is clearly independent of the assumed inclination. On this scale however, it is unclear where the peak inclination lies. The lower panels show sections through the surfaces (a) and (b), and allow the peaks to be determined (see text).

of i , choosing finally the inclination and mass pair with the highest overall entropy.

We first show how the entropy depends on the choice of i . Fig. 6(e) shows the maximum entropy values extracted from a series of mass landscapes obtained over a range of inclinations with a fixed systemic velocity of 7 km s^{-1} using our blue data. Similarly in Fig. 6(f), the maximum entropy is plotted assuming the systemic velocity of 6.5 km s^{-1} derived earlier, for the red ISIS data. For the blue arm, we obtain a value of 43° . For the red arm data, this value shifts slightly

to 42° ; just as we chose a unique value of γ based upon the relative quality of the mean profiles obtained from the blue and red data, we also chose to adopt the blue arm derived value of 43° for the inclination of RU Peg.

It is at first sight surprising that an inclination can be deduced for a non-eclipsing system. However, the inclination affects the line profile in two ways. First, the variation in the apparent width of the stellar absorption line-profile around the orbit depends on i (e.g. Shahbaz 1998); second, the way the spot bumps traverse the profile depends quite strongly

Data	K_2 (km s $^{-1}$)	K_1 (km s $^{-1}$)
Red arm, from tomogram	131.2	116.1
Blue arm, from tomogram	133.5	123.6
Direct, red arm, this paper	128.2	112.6
Friend et al. (1990)	121 \pm 2	
Stover (1981)		94 \pm 3
Kiplinger (1979)		88 \pm 10

Table 3. A comparison of the radial velocity semi-amplitudes implied by our maximum entropy results with direct measurements.

on i (for example, there would be no motion of the bump at all if the inclination were zero). The maximum entropy method disentangles this dependence and yields an inclination. As with the systemic velocity, we would ideally like to estimate all uncertainties rigorously by undertaking a full Monte Carlo study; however, we have estimated that this might take up to a month of computer time, and no-one doing Roche tomography studies has yet attempted a full error analysis.

Friend et al. (1990) find a value of $33^\circ \pm 5^\circ$ for the inclination derived by assuming a main-sequence mass-radius relation for the secondary. However, if the primary star is a carbon-oxygen white dwarf (i.e. $M_1 = 0.55\text{--}1.2 M_\odot$ – Iben 1985), then the allowed range of inclinations for RU Peg is $34^\circ\text{--}48^\circ$, which our value lies well within. The assumption that the secondary obeys a main sequence mass radius relation is also applied in Kiplinger (1979) who quotes a lower limit of 30° . Our value is, however, in good agreement with Sion & Urban (2002), who determine a value of 41° from model fitting of the disc spectrum.

The mass entropy landscapes corresponding to the above values of systemic velocity and inclination are shown in Fig. 7. From these, we derive estimates for the component masses of $M_1 = 1.08 M_\odot$ and $M_2 = 1.0 M_\odot$ for the blue data, and $M_1 = 1.04 M_\odot$ and $M_2 = 0.92 M_\odot$ for the red data. While the derived primary star mass values are quite similar, there is a greater difference between the values for the secondary star masses. We see no reason to preferentially adopt one estimate of the mass (either derived from the blue or the red data) over the other. Instead we adopt an average of these values and estimated uncertainties of $\pm 0.04 M_\odot$ for the primary masses and $\pm 0.08 M_\odot$ for the secondary masses which take into account the scatter between the values, but not any possible systematic effects; the real uncertainty is very likely to be larger.

Having determined the best-fit system parameters, it is of interest to see what radial-velocity amplitudes are implied by these values and how they compare with previous direct determinations. Because the system parameters from the blue and red data differ, we consider these data sets separately. The results are given in Table 3, where they are compared with our direct values from Section 3.2 and values from the literature.

The deduced K_2 values from the two independent datasets agree satisfactorily and are not very different from the direct value found in Section 3.2. More surprisingly, they are slightly larger than the direct value, which is not what would be expected if the difference were due to irradiation. This probably means that irradiation has no dramatic effect on the radial velocity amplitude in this long-period,

low inclination system, and that the values are consistent, implying that the uncertainties on each are about 4 km s^{-1} . While our K_2 value of $\sim 130 \text{ km s}^{-1}$ differs significantly from that found by Friend et al. (1990), we note that their data was of significantly lower resolution (at best 75 km s^{-1}) and this may account for the difference. The deduced K_1 values are rather more different from one another. If they are also assumed to be free from systematic errors, then this would indicate an uncertainty in the derived K_1 values of $\sim 5 \text{ km s}^{-1}$. However, the three values from this paper are sufficiently similar to rule out the considerably smaller values found by Stover (1981) and Kiplinger (1979).

5.2 Surface images

Fig. 5 shows the input trailed spectrum of the blue-arm LSD absorption profiles together with the computed data from Roche tomography and the corresponding residuals. The Roche tomogram produced from this trail is shown in full in the left hand panel of Fig. 8. Perhaps the most visually striking feature is the large, dark, high latitude star-spot. This is a surprising result given the intermediate resolution of the ISIS spectrograph which we had assumed would be insufficient to map spots. However, given the inclination of the system (43°), polar features would be visible throughout the whole orbit and would contribute at every phase, thereby lending themselves to detection with even relatively low resolution instruments.

Similar large high latitude spots are commonly found in Doppler imaging studies of rapidly rotating single stars and have also been recently detected in two other CVs – AE Aqr (Watson et al. 2006) and BV Cen (Watson et al. 2007a). These features are in clear contrast to sun-spots, whose locations are rarely more than 30° from the solar equator. In the case of RU Peg, we have determined that the centre of the spot lies at a latitude of $\sim 82^\circ$, and covers an area approximately 4 per cent of the total surface area of the secondary star. What causes the emergence of such high latitude star-spots? Schüssler & Solanki (1992) propose that the strong Coriolis forces dominate over the buoyancy of emerging magnetic flux tubes from deep within the convective zone and force them to follow a path almost parallel to the rotational axis. Although this conclusion was drawn for single stars, the dynamics of magnetic flux emergence is essentially the same for synchronously rotating stars. An alternative scenario of migrating star-spots has been suggested by Vogt et al. (1999), who report on the apparent clockwise spiral migration of small long-lived spots towards the pole, perhaps merging with the polar spot. Whether these migrating spots reinforce or cancel out the polar spot is of course dependent on their (as yet) unknown polarity. The star-spot in our map also appears to be deflected slightly towards the trailing edge of the star. This apparent deflection is also clear in the Roche tomograms of AE Aqr and BV Cen by Watson et al. (2006, 2007a). A comparison of the Roche tomogram of RU Peg to those of AE Aqr and BV Cen is shown in Fig. 9 along with a preliminary map of V426 Oph by Watson et al. (2007b). Is this a common feature of tidally distorted rapidly rotating stars? If so, what is the exact mechanism that produces it? Perhaps it is caused by the orbital motion of the binary. Interestingly, there is no such high-latitude spot present in the V426 Oph map, though

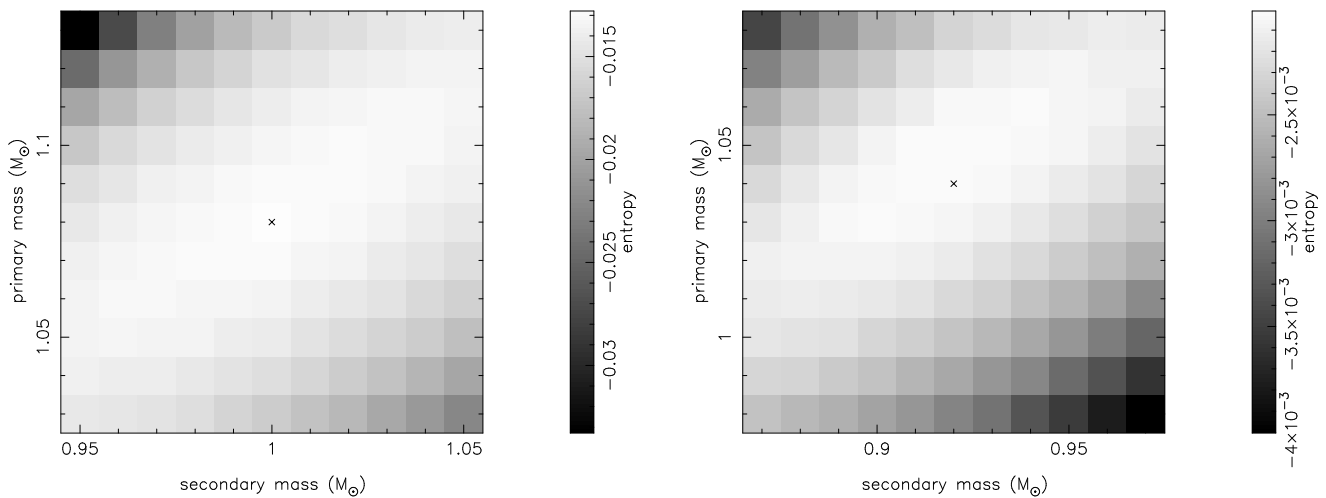


Figure 7. *Left* – Entropy landscape for the RU Peg blue data, assuming an inclination of 43° and a systemic velocity of 7 km s^{-1} . Black pixels represent mass combinations for which no acceptable solution could be found. The black cross indicates the entropy peak, corresponding to primary and secondary masses of $M_1 = 1.08 M_\odot$ and $M_2 = 1.0 M_\odot$. *Right* – Entropy landscape for the RU Peg red data, assuming an inclination of 42° and a systemic velocity of 6.5 km s^{-1} . The component masses giving rise to the maximum entropy are $M_1 = 1.04 M_\odot$ and $M_2 = 0.92 M_\odot$.

this system was caught in an extended (and unusual) quiescent state, where its regular outbursting behaviour had essentially halted for over a year. Thus, if magnetic activity is responsible for the behaviour of CVs then the map of V426 Oph may not be representative of the system as it would normally appear.

Given the resolution of our RU Peg data, this is probably the best that can be produced by applying LSD. The amplitude variation in the mean line profile due to small scale spots is too low to be confidently detected. However, Fig. 8 also seems to suggest the presence of smaller amplitude features at lower latitudes (labelled *A*, *B* and *C*). These could possibly be more star-spots at the limit of detectability (they seem to be hinted at in the red tomograms too) or they could simply be artefacts of unknown cause. The other main feature of the map is the dark region around the L_1 point, best seen in the image at phase 0.5 in Fig. 8. While this could be due to a large spot, given the proximity of this region to a hot irradiating source (particularly prominent if the white dwarf is especially hot) it is more likely to be due to irradiation. Such irradiation patterns have been observed in both high and low resolution maps. The irradiation in RU Peg was previously mapped by Davey (1994) using sodium flux deficit measurements. The map produced showed an anomalous region, centred at phase 0.3 on the trailing hemisphere and extending some way towards the back of the star. Indeed, this feature extended well beyond the terminator such that Davey (1994) concluded that it was highly unlikely to be caused entirely by heating, and instead speculated that it might be caused by magnetic activity on the secondary star. Our maps show no sign of this feature, with the accretion pattern being symmetric. However, the maps of Davey (1994) have no latitude discrimination, so it is possible that what was being detected was a superposition of symmetric heating and a high latitude spot that was located on the trailing hemisphere.

The right hand panel of Fig. 8 shows the Roche tomogram created using the red-arm data. Again, prominent

are the off-axis polar spot and irradiation pattern, confirming their reality, although in this map the two features are rather more blended together. Curiously, there does seem to be some non-uniformity in the irradiation pattern with less ionisation on the leading hemisphere side of the L_1 point. It is difficult to explain this feature given the lower signal to noise of the red profiles and is dismissed as most likely to be an artefact.

Simulating the effects of poor relative flux calibration

Roche tomography maps relative line fluxes, and as such, the input data are assumed to have an accurate relative flux calibration. In practice, this is achieved by either obtaining simultaneous photometric observations, or by observing a comparison star on the same slit as the main target. In this case we used a comparison star on the slit (as described in Section 2.1) to correct for slit-losses. However, the trailed spectrum of the LSD profiles shown in Fig. 5 clearly shows some imperfections in the relative scaling of the parent spectra, despite multiple attempts to remove this effect during the data reduction stages.

In order to assess the potential impact this has on the resultant Roche maps, a simulation has been carried out using a test image featuring a number of star-spots at a range of longitudes. A very low noise trailed spectrum was then computed, assuming a negligible intrinsic profile and an instrumental resolution of 20 km s^{-1} . Reconstruction of the synthetic trailed spectrum, fitting to a χ^2 of 1.0, showed that all the main features present in the test image were successfully reconstructed. Next, the trailed spectrum was given a 10% error in the relative profile line flux and reconstructions were once again carried out to the same value of χ^2 . Again, the reconstructions faithfully reproduced the star-spot features, but the stellar surface has an additional noise pattern superimposed upon it. It is found that this low level noise is removed by slightly under-fitting the data, to a χ^2 of 1.5. Therefore, just as incorrect input parameters have

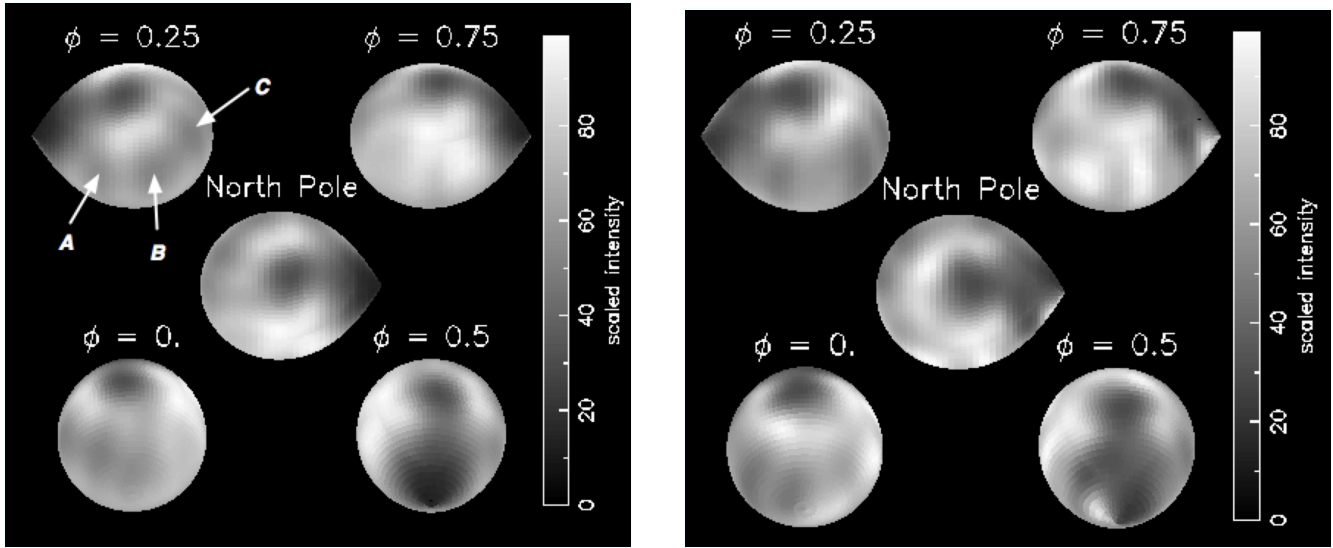


Figure 8. *Left* – Roche tomogram of RU Pegasi derived from blue-arm ISIS data. The intensity scale is adjusted so that dark scales represent regions of lower absorption. The map is presented as the observer would see it at an inclination of 43° except for the central image, where the observer is directly above the north pole. *Right* – Roche tomogram of RU Pegasi derived from red-arm ISIS data. The grey scale and viewpoint are the same as in the blue-data map.

a known effect upon the level of structure in a Roche map, imperfect relative flux scaling also produces image artefacts that can be identified. These simulations give us more confidence that both the irradiation pattern (in general, we do not believe the asymmetry apparent in the red data) and the high-latitude spot are real features. However, the lower resolution of the RU Peg data means that no smaller-scale features can be reliably identified (cf. Fig. 9).

6 $H\alpha$ EMISSION LINE DOPPLER TOMOGRAPHY

Doppler tomography is a powerful technique for mapping the emission lines in CVs. Since our RU Peg data cover most of the orbit during an outburst, and show prominent Balmer emission lines, it seems logical to construct a Doppler tomogram. Here, we have used the code of Spruit (1998) to map the distribution of $H\alpha$ in velocity space. In this reconstruction, the Roche lobe geometry has been set by specifying the values for the orbital elements and component masses derived earlier.

It is immediately obvious that there is no strong disc emission present in the map; this is probably a result of the system being in outburst, and the disc becoming optically thick, so that the lines switch from emission to absorption. The most striking emission feature is the very bright region at the velocity of the secondary star. The brightest pixels are found at a position exactly where the inner hemisphere of the secondary lies (also marked on the image). This is in excellent agreement with our Roche tomograms which show symmetric irradiation about the L_1 point.

7 CONCLUSIONS

The Roche tomograms of RU Peg show prominent irradiation of the inner hemisphere of the secondary star. The

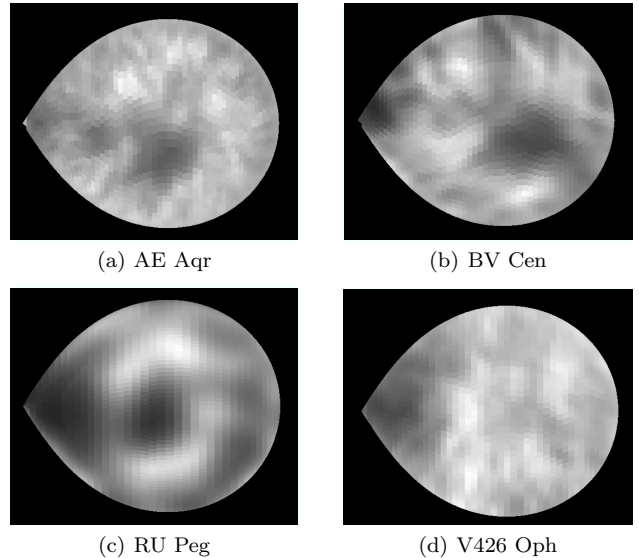


Figure 9. Comparison of published multi-line Roche tomograms with the RU Peg map in this work. The maps of AE Aqr and BV Cen both show the large high latitude spot present in the RU Peg map while, interestingly, the provisional V426 Oph map does not. Note that the generally smoother appearance of the RU Peg map is caused by the fact that the data are of lower spectral resolution than for the other three maps, and so cannot reveal small-scale features; much of the apparent ‘noise’ in the other maps is probably caused by small spots.

degree of irradiation found is of no surprise because RU Peg was caught near its peak magnitude during outburst. Unlike the Na-flux deficit mapping of RU Peg carried out by Davey (1994), we see no asymmetry in the irradiation pattern, nor do we see any evidence for irradiation extending beyond the terminator towards the back of the star.

The Roche tomograms also show a near-polar spot cen-

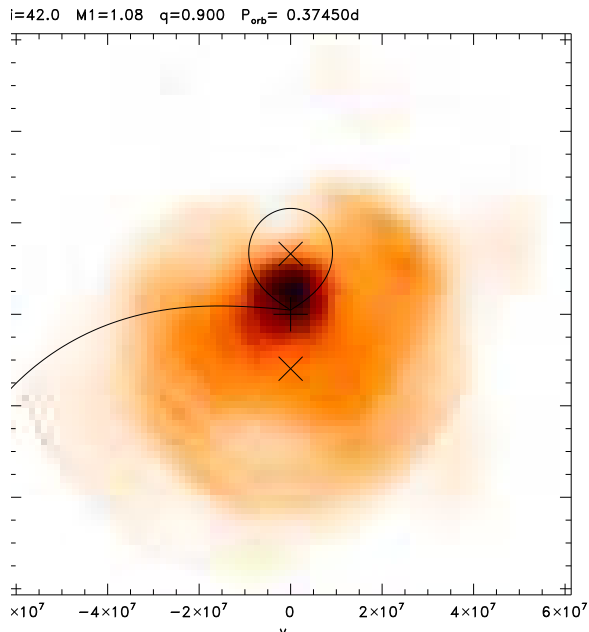


Figure 10. Doppler tomogram of RU Peg in the light of H α emission. Shown are the centres of mass of the primary and secondary stars (crosses) and the surface of the Roche-lobe shaped star. The ballistic mass transfer stream is also shown.

tred at a latitude of 82° and covering an estimated 4 per cent of the stellar surface. While the resolution of the data is too low to place any limit on the overall spot filling factor across the star, the presence of a large spot comparable to the largest spots seen on BV Cen and AE Aqr suggests that RU Peg is also highly magnetically active. As with the prominent high latitude spots found on AE Aqr and BV Cen, the spot on RU Peg also lies towards the trailing hemisphere. (Though we note that, at a latitude of 82° , the spot on RU Peg is distinctly more ‘polar’ than the prominent spots on both AE Aqr and BV Cen which lie at a latitude of $\sim 65^\circ$.) Whether this is a common feature of all CV donor stars and indicative of a preferred longitude for magnetic flux emergence caused by either orbital or tidal effects remains to be seen.

Finally, the spot on RU Peg almost ‘merges’ with the irradiated region. Since spotted and irradiated regions both appear as apparent absorption-line flux deficits, we speculate that this may be able to explain the asymmetric irradiation patterns found by Na-flux deficit mapping of CV donors (see Davey 1994; Davey & Smith 1992; Davey & Smith 1996; Catalan et al. 1999). Instead of just indicating irradiated regions, could these maps also be affected by the presence of large spots which are shifted towards one hemisphere? With the comparatively low-resolution afforded by these maps, it is feasible that large spotty regions could become blended with the irradiated zone. This inability to distinguish between large spots and irradiated regions in such methods could lead to maps suggestive of an asymmetric irradiation pattern which may appear to extend beyond the terminator depending on the location of the spot. This explanation has the advantage of being able, in principle, to explain asymmetries of either sign unlike previous explana-

tions (see Smith 1995 for a review of the early maps and their interpretations).

ACKNOWLEDGMENTS

Alex Dunford was supported by a PPARC studentship. The William Herschel Telescope is operated by the Isaac Newton Group at the Observatorio del Roque de los Muchachos of the Instituto de Astrofísica de Canarias. The authors thank Tom Marsh for the use of his PAMELA and MOLLY software packages. We acknowledge the use of the Vienna Atomic Line Database (VALD) for obtaining our atomic line lists. Finally, we thank Roger Pickard, Director of the BAA VSS, for arranging amateur photometric observations that covered the period of our observing run.

REFERENCES

- Ak T., Ozkan M. T., Mattei J. A., 2001, *A&A*, 369, 882
- Applegate J. H., 1992, *ApJ*, 385, 621
- Barnes J. R., 1999, PhD thesis, University of St. Andrews
- Catalan M. S., Schwöpe A. D., Smith R. C., 1999, *MNRAS*, 310, 123
- Claret A., 1998, *A&A*, 335, 647
- Collier-Cameron A., Unruh Y. C., 1994, *MNRAS*, 269, 814
- Collins II G. W., Truax R. J., 1995, *ApJ*, 439, 860
- Davey S., Smith R. C., 1992, *MNRAS*, 257, 476
- Davey S., Smith R. C., 1996, *MNRAS*, 280, 481
- Davey S. C., 1994, PhD thesis, University of Sussex
- Dhillon V. S., Marsh T. R., 1993, in Regev O., Shaviv G., eds, *Cataclysmic Variables and Related Physics 2nd Technion Haifa Conference, Infrared Spectra of Cataclysmic Variables*. Institute of Physics Publishing, Bristol, p. 34
- Donati J.-F., Collier Cameron A., 1997, *MNRAS*, 291, 1
- Evans D. S., 1967, in Batten A. H., Heard J. F., eds, *Determination of Radial Velocities and their Applications Vol. 30 of IAU Symposium, The Revision of the General Catalogue of Radial Velocities*. p. 57
- Friend M. T., Martin J. S., Smith R. C., Jones D. H. P., 1990, *MNRAS*, 246, 654
- Gray D. F., 1992, *The Observation and Analysis of Stellar Photospheres*. ISBN 0521408687. Cambridge, UK: Cambridge University Press, June 1992.
- Harrison T. E., Johnson J. J., McArthur B. E., Benedict G. F., Szkody P., Howell S. B., Gelino D. M., 2004, *AJ*, 127, 460
- Holzwarth V., Schüssler M., 2003, *A&A*, 405, 303
- Horne K., 1986, *PASP*, 98, 609
- Horne K., Wade R. A., Szkody P., 1986, *MNRAS*, 219, 791
- Iben Jr. I., 1985, *QJRAS*, 26, 1
- Kiplinger A. L., 1979, *AJ*, 84, 655
- Kraft R. P., 1962, *ApJ*, 135, 408
- Kraft R. P., 1967, *ApJ*, 150, 551
- Kupka F., Piskunov N., Ryabchikova T. A., Stempels H. C., Weiss W. W., 1999, *A&AS*, 138, 119
- Kupka F. G., Ryabchikova T. A., Piskunov N. E., Stempels H. C., Weiss W. W., 2000, *Baltic Astronomy*, 9, 590
- Mestel L., 1968, *MNRAS*, 138, 359
- Richman H. R., Applegate J. H., Patterson J., 1994, *PASP*, 106, 1075

- Rutten R. G. M., Dhillon V. S., 1994, *A&A*, 288, 773
 Scharlemann E. T., 1982, *ApJ*, 253, 298
 Schüssler M., Solanki S. K., 1992, *A&A*, 264, L13
 Shahbaz T., 1998, *MNRAS*, 298, 153
 Sion E. M., Urban J., 2002, *ApJ*, 572, 456
 Smith D. A., Dhillon V. S., 1998, *MNRAS*, 301, 767
 Smith R. C., 1995, in Buckley D. A. H., Warner B., eds, *Cape Workshop on Magnetic Cataclysmic Variables Vol. 85 of ASP Conference Series, Secondary Stars and Irradiation*, p. 147
 Spruit H. C., 1998, *ArXiv astro-ph/9806141*
 Spruit H. C., Ritter H., 1983, *A&A*, 124, 267
 Stover R. J., 1981, *ApJ*, 249, 673
 Strassmeier K. G., Fekel F. C., 1990, *A&A*, 230, 389
 Vogt S. S., Hatzes A. P., Misch A. A., Kürster M., 1999, *ApJS*, 121, 547
 Wade R. A., 1982, *AJ*, 87, 1558
 Warner B., 1995, *Cataclysmic variable stars*. Cambridge Astrophysics Series, Cambridge, New York: Cambridge University Press
 Watson C. A., 2002, PhD thesis, University of Sheffield
 Watson C. A., Dhillon V. S., 2001, *MNRAS*, 326, 67
 Watson C. A., Dhillon V. S., Rutten R. G. M., Schwöpe A. D., 2003, *MNRAS*, 341, 129
 Watson C. A., Dhillon V. S., Shahbaz T., 2006, *MNRAS*, 368, 637
 Watson C. A., Steeghs D., Dhillon V. S., Shahbaz T., 2007b, *AN*, 328, 813
 Watson C. A., Steeghs D., Shahbaz T., Dhillon V. S., 2007a, *MNRAS*, 382, 1105
 Webb N. A., Naylor T., Jeffries R. D., 2002, *ApJL*, 568, L45

This paper has been typeset from a \LaTeX file prepared by the author.